



Tungsten carbide nanowalls as electrocatalyst for hydrogen evolution reaction: New approach to durability issue

Young-Jin Ko ^{a,b}, Jung-Min Cho ^{a,b}, Inho Kim ^a, Doo Seok Jeong ^a, Kyeong-Seok Lee ^a, Jong-Keuk Park ^a, Young-Joon Baik ^a, Heon-Jin Choi ^{b,*}, Wook-Seong Lee ^{a,*}

^a Center for Electronic Materials, Korea Institute of Science and Technology, Seongbuk-gu, Seoul, 136-791, Republic of Korea

^b Advanced Materials Science and Engineering, Yonsei University, Seodaemun-gu, Seoul, 120-749, Republic of Korea

ARTICLE INFO

Article history:

Received 22 June 2016

Received in revised form 18 October 2016

Accepted 31 October 2016

Available online 1 November 2016

Keywords:

Hydrogen evolution

Tungsten carbide

Nanowall structure

Electrochemical durability

Turnover frequency

ABSTRACT

We report a new approach to the durability issue in tungsten carbide electrocatalyst for hydrogen evolution reaction (HER), in a form radically differing from that of the conventional nanoparticle approach: the WC nanowalls, bottom-up grown by a plasma-assisted deposition on Si wafer. The pristine nanowall was highly crystalline and its surface was smooth in atomic scale, which enabled a superior durability in HER environment: no oxidation occurred at prolonged cycling (10,000 cycles) in the HER environment, even without additional functionalization or modification. The electrochemical activity, as presented by Tafel slope and turnover frequency (TOF), was as excellent as those of the best data in the literature.

© 2016 Elsevier B.V. All rights reserved.

1. Introduction

Molecular hydrogen has been actively studied since 70s, as post-hydrocarbon energy carrier owing to its numerous benefits: the largest energy density per unit mass, clean byproduct (water), in contrast to the hydrocarbon fuel with CO₂ byproducts [1], and global abundance. On the other hand, the hydrogen usually exists as compounds, from which the hydrogen should be isolated. The most widely adopted isolation process is the steam reforming process, but it relies on the fossil fuels, which suffers the CO₂ generation [2]. Among the clean, renewable and CO₂-free hydrogen generation processes, one of the most promising processes is the water electrolysis [3], which employs the two half-cell reactions for electrochemical water splitting, *i.e.* the hydrogen evolution reaction (HER) and oxygen evolution reaction (OER) [4]. The strongest catalyst for HER is Platinum, but its global resource is limited, which acutely falls short of the global energy demand. Consequently a strong demand is put on the alternative catalyst derived from the earth-abundant element, but it should satisfy (1) the electrochemical activity *i.e.* low overpotential, and (2) the durability in operating condition.

Tungsten carbide has been actively investigated [4–6], due to its Pt-like d-band DOS(density of states) [7–9], cost-effectiveness [7,10], mechanical strength as well as good conductivity [10]. But it still suffers some critical drawbacks: majority of studies employed nanoparticles form, which suffered sintering during synthesis, consequent coarsening, and eventual loss of activities when used in pristine form [7,11]. Moreover, such nanoparticle-based processes suffered oxide-passivation in HER environment, again with undesirable loss in the electrocatalytic activities and hence the poor durability [10]. Efforts were made, *e.g.* by adopting SiO₂ template to prevent sintering [7], surface modification or heteroatom hybridization to prevent oxidation [12,13]. However, such approaches still relied on the nanoparticles, of which the extreme-curvature surface is inherently defective and unstable [14], unless they are modified, *e.g.* by aforementioned means. Even for the nanoparticles with superior performances, some performance degradation still persisted at the prolonged exposure to the HER environment [7], probably due to oxide passivation. Thus, the oxide-passivation issue still hampers the successful progress of the tungsten carbide electrocatalyst.

Here we report a simple but radically differing approach to this issue. Instead of modifying the nanoparticles, we adopted tungsten carbide *nanowalls* which we have recently reported [15], synthesized by a plasma-assisted deposition, which is now in commercial scale [16]. It was important that the nanowalls were highly crystalline and were smooth in atomic scale on their surfaces [15],

* Corresponding authors.

E-mail addresses: hjc@yonsei.ac.kr (H.-J. Choi), wsleemk@gmail.com (W.-S. Lee).

in contrast to the highly disordered pristine surface of the conventional tungsten carbide nanoparticles, as will be further shown here; it might accordingly enhance the electrocatalytic stability or durability. A further motivating observation was that the nanowalls collectively formed a nanoporous network [15], which might allow effective access of the HER solution. However, relevant studies were not reported so far. Here we investigated such possibilities, as a comparative study on the two contrasting types of tungsten carbide thin films, comprised of nanowalls and nanocrystalline grains, respectively, grown on nanodiamond-coated Si wafer substrates [15], which will highlight the origin of the superior HER performances of the former in its pristine form, as comparable to some best data in the literatures of the conventional tungsten carbide nanoparticles with additional surface modifications.

2. Experimental

2.1. Preparation of WC/NCD film

The tungsten carbide nanowall film was synthesized on the NCD-coated Si wafer by the direct current plasma assisted CVD (DC-PACVD) using surface-carburized tungsten cathode [15]. The substrate was exposed to the hydrogen plasma in the CVD chamber. The total hydrogen gas flow rate and the chamber pressure were 150 SCCM and 100 Torr, respectively. Details of the synthesis procedure, growth mechanisms, and preliminary characterizations were reported elsewhere [15].

2.2. Physical characterization

Transmission electron microscopy (TEM) and high-resolution transmission electron microscopy (HR-TEM, FEI Co., Titan 300 kV) were employed to observe structure of synthesized WC. The surface morphology of the WC/NCDs was analyzed by scanning electron microscope (SEM, FEI Co., Nova 200 NanoSEM) at an acceleration voltage of 10 kV. The distribution of the oxide phase was analyzed by the Fourier-masked scanning TEM [17]. The surface chemistry of WC was characterized by the x-ray photoelectron spectroscopy (XPS, Ulvac Co., PHI 5000 Versaprobe). Wide angle X-ray diffraction (XRD, Rigaku Co., D/MAX-2500H) was used to examine the crystal structure and identify the nature of carbide and oxides. The roughness of WC surface was analyzed by non-tapping mode atomic force microscope (Park system Co., XE-100).

2.3. Electrochemical analysis and durability test

All electrochemical measurements were performed with a VSP Potentiostat/Galvanostat (Bio-logic Co., France). The experiment was performed in a three-compartment electrochemical cell in 0.5 M H₂SO₄. The Hg/Hg₂SO₄ electrode and graphite rod were used as the reference electrode and the counter electrode, respectively. It was calibrated with respect to reversible hydrogen electrode (RHE), in the high purity H₂-saturated electrolyte with a Pt wire as the working electrode. CVs were run at a scan rate of 1 mV/s, and the average of the two potentials at which the current crossed zero was taken to be the thermodynamic potential for the hydrogen electrode reactions, i.e. in 0.5 M H₂SO₄, E (RHE)=E (SCE)+0.702 V. All the potentials reported in the present study are against RHE.

The electrochemical activation was carried out employing the cyclic voltammetry of 4000 cycle from -0.3 V to 0 V (RHE) with 10 mV/s scan rate. The linear sweep voltammetry was carried out with 5 mV/s scan rate. The durability test was carried out using cyclic voltammetry of 10,000 cycle from -0.5 V to 0.2 V (RHE) with 10 mV/s scan rate. The electrochemical impedance spectroscopy was carried out at open circuit voltage from 10⁵Hz down to 10⁻²Hz with 10 mV AC amplitude. In order to estimate the effective surface

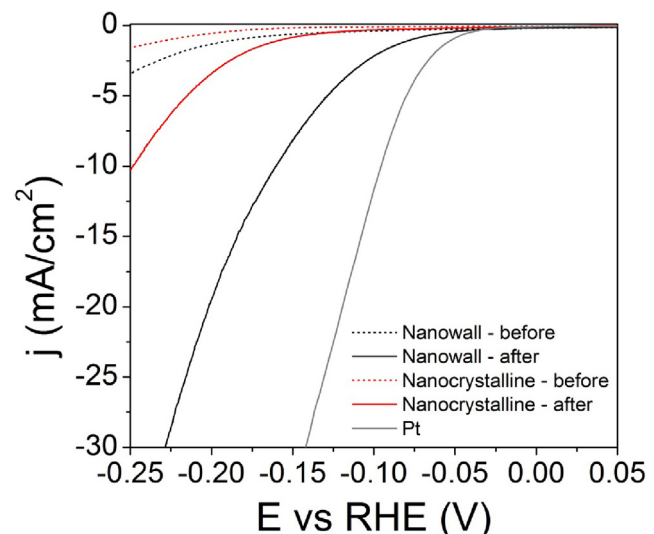


Fig. 1. Polarization curves of HER for WC nanowall and WC nanocrystalline films, before and after the initial cyclic cleaning.

Table 1
HER activity comparison of WC nanowall and WC nanocrystalline films.

Material	Onset potential (V)	Overpotential @ 10 mA/cm ² (mV)	Current density @ 0.25 V (mA/cm ²)
WC nanocrystalline	-0.102	248	-10.31
WC nanowall	-0.052	160	-40.10
Pt	-0.005	95	-83.85

area of the samples, the double-layer capacitance (C_{dl}) was analyzed by cyclic voltammetry in a potential range of 0.1–0.2 V with various scan rates (20, 40, 60, 80, and 100 mV/s).

3. Results and discussion

Fig. 1 shows the LSV (Linear Sweep Voltage) curve [corrected of the ohmic potential drop (IR)] of the WC nanowall sample at its HER, before and after the 4000 cycles of the initial cyclic cleaning (ohmic potential correction details: Statement S1 and Fig. S1). While the cleaning enhanced the activities for both samples, the enhancement was much stronger for the nanowall sample: the results were summarized in **Table 1**. The onset potential and the current density of the nanowall sample were superior to those of nanocrystalline sample: the overpotential (η) of the former at the cathodic current density around 10 mA/cm² was 88 mV lower than that of the latter. Origin of such strongly differing HER response to the initial cleaning could be inferred from the W 4f XPS spectra (**Fig. 2**). While tungsten oxide peaks were drastically reduced for the nanowall sample by the cleaning (**Fig. 2a, b**), the peaks persisted to a substantial extent for the nanocrystalline sample (**Fig. 2c, d**). The carbide peaks changed little (**Fig. 2a, b**) in accord with previous reports [18,19]. The corresponding responses of the carbon peaks strongly differed also (**Fig. 3**: C 1s XPS analyses). While the graphitic carbon peak drastically dropped after cleaning for the nanowall sample (**Fig. 3a, b**), it changed little for the nanocrystalline sample (**Fig. 3c, d**). Such graphitic carbon layer was reported to damage the electrochemical activity [20]. While the enhanced HER activities should be attributed to such removal of oxide and carbon layer, which was reported to be caused by the dissolving action of the sulfuric acid in the initial cycling, microscopic observations revealed further details of the cleaning-induced changes: SEM (**Fig. 4**, S2), HR-TEM (**Fig. S3**: nanowall; **Figs. S5, S6** and **S8**: nanocrystalline) and corresponding Fourier-masked HR-TEM (**Fig. S4**: nanowall; **Figs. S7,**

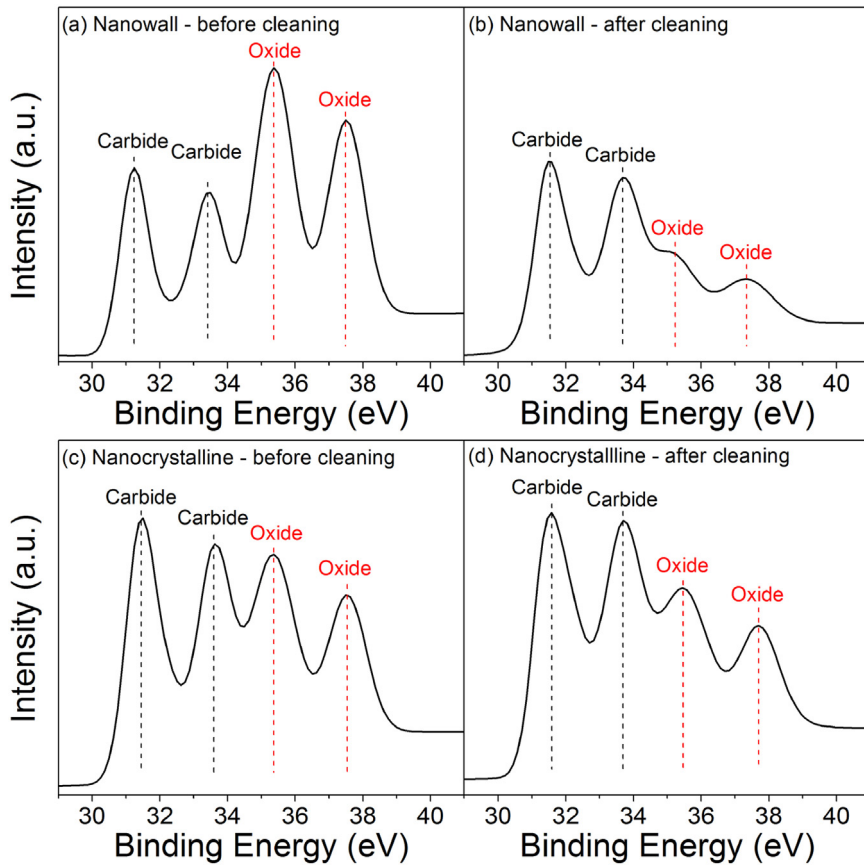


Fig. 2. W 4f XPS spectra of WC nanowall and WC nanocrystalline films.

S9: nanocrystalline) [17]. The HR-TEM, Fourier-masked HR-TEM pictures supported the differing oxide removal behaviors of the two samples. The oxides persisted substantially at the grain boundary of the nanocrystalline sample, while in nanowall sample the oxide was scarcely observed after cleaning. The SEM images indicated that the nanowalls became finer, and that the sample thickness decreased; in the nanocrystalline sample also, the corresponding morphological changes were observed. Thus we have shown that the cyclic cleaning removed oxide and carbon layers much more efficiently from the nanowall sample, to eventually expose the pristine tungsten carbide layers, in contrast to the nanocrystalline sample.

Next important issue was the durability: both samples were subjected to prolonged cycling (10,000 cycles, which was the longest cycling reported so far, as shown later) subsequent to the initial cleaning, followed by XPS analyses (Fig. 5). The impact of the 10,000 cycle test on the polarization curves accordingly differed greatly (Fig. 6). The change was negligible for the nanowall sample (Fig. 6a), while the strong deterioration occurred for the nanocrystalline sample (e.g. overpotential changed by 14 mV at the current density of 10 mA/cm^2 , Fig. 6b). Such superior durability of the pristine nanowall sample was compared with some of the best data in the literatures, which adopted the modified nanoparticles (Table 2): while the conventional modified nanoparticles were resistant to the relatively weak acidic media ($0.05 \text{ M H}_2\text{SO}_4$, $\text{pH} = 1$), in stronger acidic media their overpotentials increased significantly, probably due to the induced oxide-passivation. It was remarkable that the present *pristine* nanowall sample showed no degradation even in the acidic media as strong as $0.5 \text{ M H}_2\text{SO}_4$, for such prolonged time (10,000 cycles) in the potential range of -0.5 to 0.2 V . The intriguing origin of such superior durability could be analyzed from the

XPS analyses (Fig. 5). Relative to the initial cyclic-cleaned state, the oxide peak intensity change was negligible for the nanowall sample (Figs. 5a, 2b), while that for the nanocrystalline sample was significant (Figs. 5c, 2d). Since the graphitic carbon peaks remained similar for both samples (Figs. 3b, 5b vs Figs. 3d, 5d), the superior durability of the nanowall sample was attributed to its superior oxidation resistance in the HER environment.

The intriguing origin of such superior durability could be considered by microstructural comparison on the two samples. The most important was the existence of the nanoscale grain boundaries in the nanocrystalline sample (Fig. S5: the network of bright contrast, Figs. S6, S8 and S12: the disordered region with brighter contrast). Each grains in the nanocrystalline sample (the darker granular domains surrounded by the brighter disordered grain boundary network) were analogous to the individual pristine nanoparticles adopted in the previous studies [7,21], in their quasi-spherical shapes with extreme nano-scale curvature. The extensive oxide phase was observed in the grain boundaries of the nanocrystalline sample, rather than in the grain interior (compare the grain boundary area in Fig. S12: HR-TEM with the marked region in Fig. S13: Fourier-masked HR-TEM). By contrast, HR-TEM image of the nanowalls after the durability test showed little change of the state, concerning the oxide (Figs. S10, S11, no oxide found in accord with the aforementioned XPS analyses). Such observations might provide an important insight for the durability issue, if one considered the similarity between the present nanocrystalline sample and the conventional pristine nanoparticles: the individual nanograins of the former was surrounded by the highly defective/disordered grain boundaries, while the latter (nanoparticles) was enclosed in their extreme-curvature surfaces [22], which was also known to be highly defective and unstable in the pristine state [23,24]. Like-

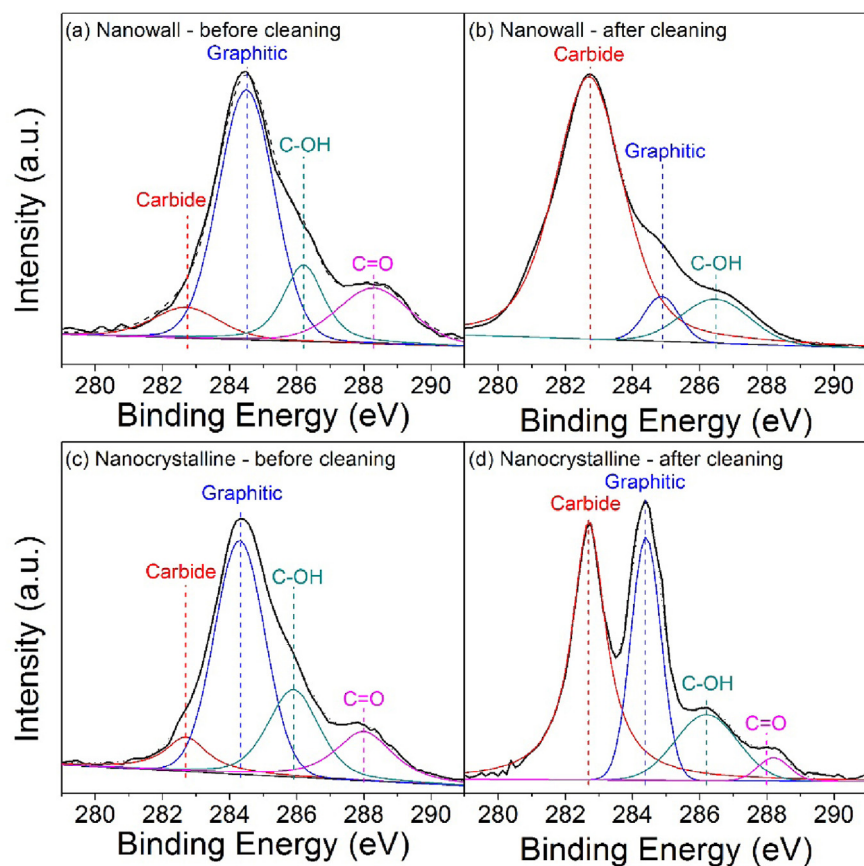


Fig. 3. C 1s XPS spectra of WC nanowall and WC nanocrystalline films.

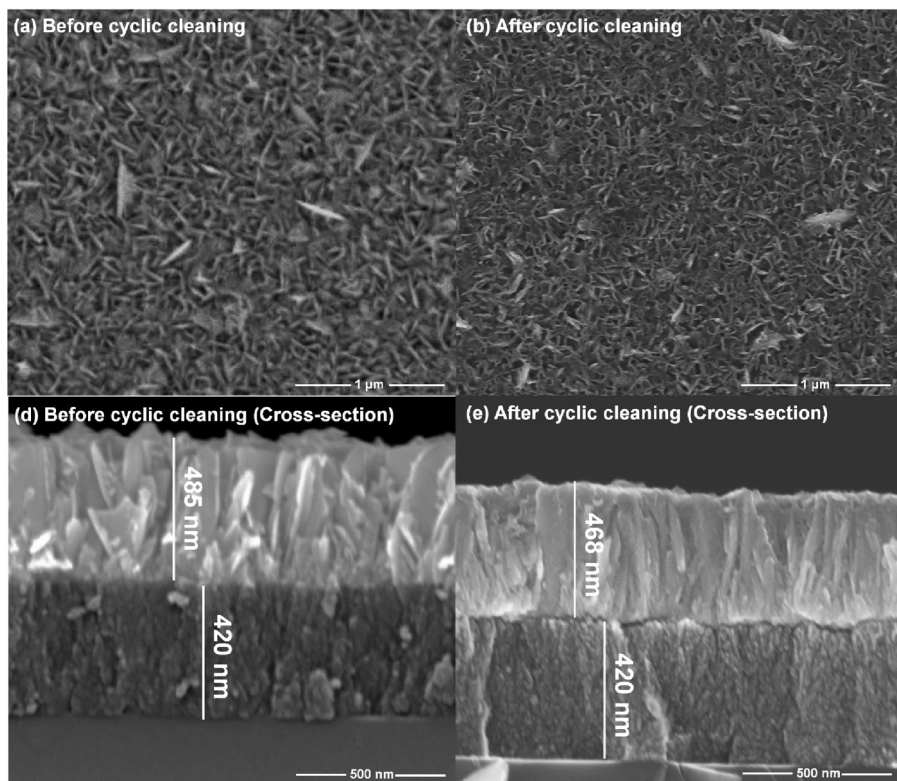


Fig. 4. SEM images of WC nanowall film (a, c) before, (b, d) after cyclic cleaning.

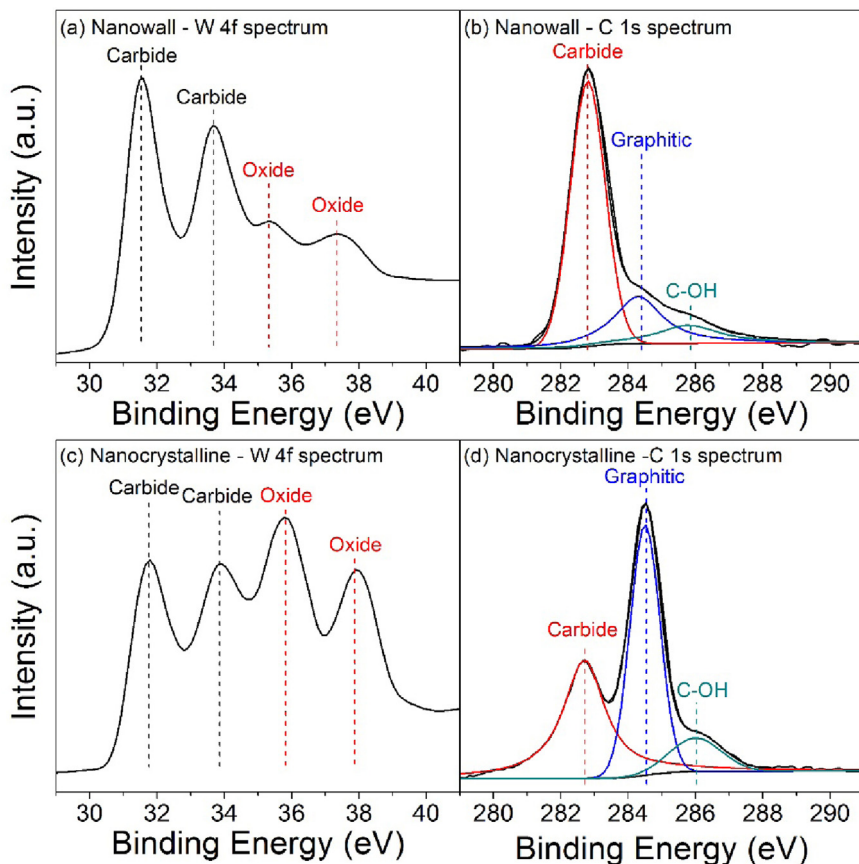


Fig. 5. XPS spectra of (a, b) WC nanowall and (c, d) WC nanocrystalline films after the durability test.

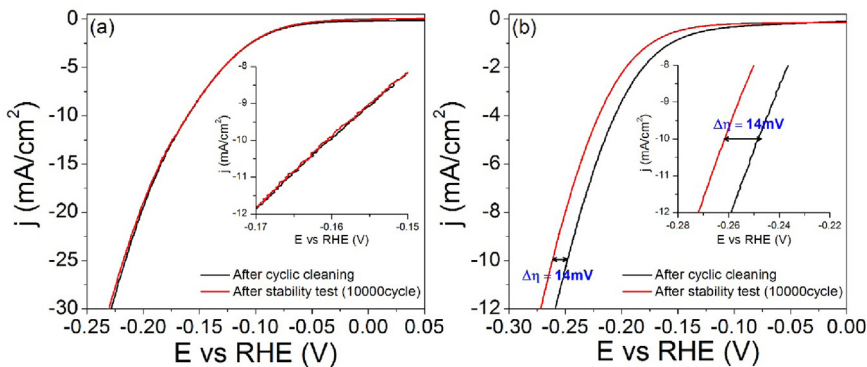


Fig. 6. Polarization curves of (a) WC nanowall and (b) WC nanocrystalline films before (red line) and after (black line) durability test. (For interpretation of the references to color in this figure legend, the reader is referred to the web version of this article.)

Table 2

The electrocatalytic activity and durability of the WC nanowall and WC nanocrystalline films as compared with the WC electrodes in the literatures.

Material	Tafel slope (mV/dec)	Onset potential (V)	Durability			
			Solution	Potential range	Cycle	Overpotential change
Fe-WCN nanoparticle [12]	47.1	-0.1	pH 1 H ₂ SO ₄	-0.3 to 0.5 V	3000	none
WC nanoparticle/Carbon Black [7]	-	-	0.5 M H ₂ SO ₄	-0.3 to 0.6 V	3000	10 mV increase
WC nanoparticle/CNT [35]	122	-	pH 1 H ₂ SO ₄	-	1000	none
WC nanocrystal [13]	65	-	0.1 M HClO ₄	-0.5 to 0.3 V	10,000	19 mV increase
WC nanocrystal [21]	84	-0.1	0.5 M H ₂ SO ₄	-0.3 to 0.1 V	800	none
W ₂ C microsphere [36]	118	-0.05	-	-	-	-
WC commercial [36]	73	-0.1	-	-	-	-
WC nanocrystalline	83	-0.102	0.5 M H ₂ SO ₄	-0.5 to 0.2 V	10,000	14 mV increase
WC nanowall	67	-0.052	0.5 M H ₂ SO ₄	-0.5 to 0.2 V	10,000	none

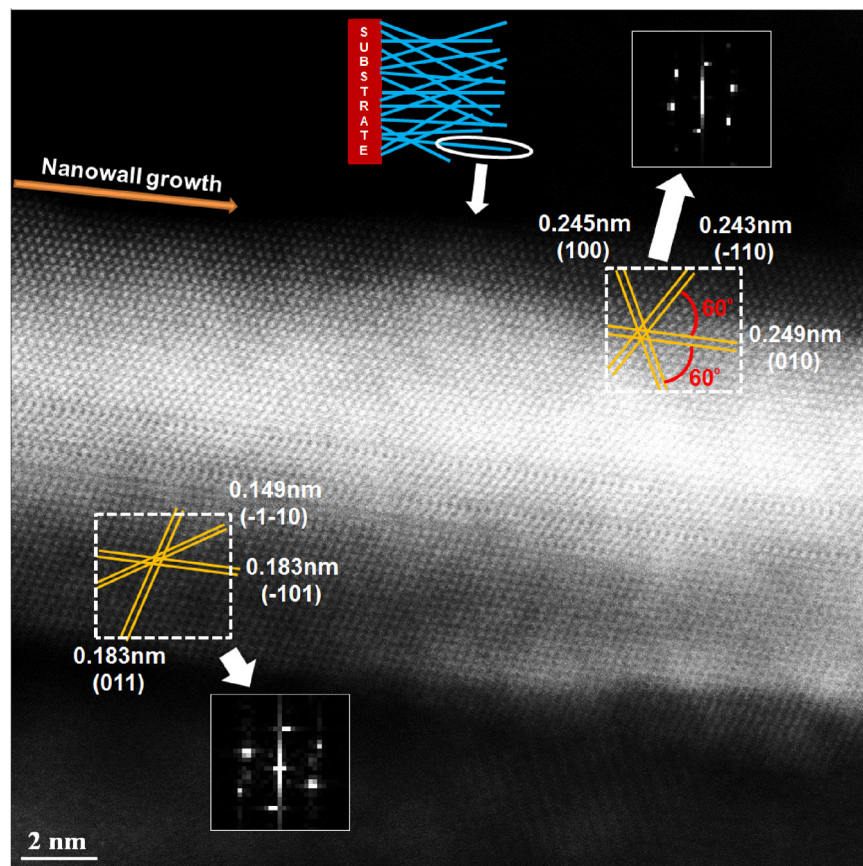


Fig. 7. Cross-sectional scanning HR-TEM image of a WC nanowall after cleaning. A member of the {001} basal plane family, i.e. the (010) plane, as indicated by the guiding lines in the upper half of the picture, were approximately parallel to the longitudinal direction of the vertically aligned nanowall growth. A multiple twin planes were observed between the upper and lower half of the flake cross-sections. The insets show the SAED patterns of the respective regions. Note the atomically smooth surface region of the cross-sectional image, as well as the high crystalline perfection throughout the cross-section.

wise, the oxidation resistance of tungsten carbide was reported to be enhanced by its crystalline perfection [10]. Indeed, the scanning HR-TEM image of the nanowall after the cleaning (Figs. 7, S14) indicated not only the absence of the disordered grain boundaries, but also the atomically smooth nanowall surface extending from its interior with high crystalline perfection, with a {001} basal plane aligned nearly parallel to the nanowall face. The microstructures of the nanowall surface after the cyclic cleaning was observed by the plane-view and the cross-sectional SEM (Figs. S15–S17); the porous structure generated by the interlinked nanowalls (Figs. S15–S16) as well as the cross sectional columnar structure of the walls (Fig. S17) were obvious.

By contrast, the nanocrystalline sample (Figs. S5, S6, S8, and S12; HR-TEM) demonstrated the extreme nanoscale surface curvature of each grains, enclosed in the network of the relatively thick, disordered grain boundaries. Such disordered surface of, or boundaries between, the grains should be obviously unstable relative to that of nanowall with atomically flat/smooth surface, and hence should be much more prone to oxidation in the prolonged cycling. Such line of reasoning was further supported by the oxide remaining exclusively at the grain boundary region after the cyclic cleaning (Figs. S8, S9) as well as after the durability test (Figs. S12, S13).

In addition, it would be instructive to consider such issue of drastically differing oxidation resistance in crystalline orientation perspectives. Recall that the individual nanowall crystals were comprised of a set of layered basal planes which were aligned more or less parallel to their longitudinal growth direction, so that the nanowall surface coincided with the basal plane (Fig. 7). Note that the basal planes of hexagonal lattices are the lowest-index plane, i.e.

the most-close-packed plane. By contrast, the set of layered basal planes in each nanocrystalline grains were randomly oriented with respect to their extreme-curvature surfaces (Fig. S8), so that the set of basal planes comprising each nanocrystalline particle should inevitably intersect the particle surface at rather large angles, so that rather higher-index planes would be exposed at the particle surface, which should be much less close-packed. It is well-known that the most-close-packed planes is the lowest in the broken bonds numbers when exposed as the crystal habit plane, with accordingly low chemical activity, while the opposite is true for other less-close-packed planes [25,26]. It strongly suggested that the stronger oxidation resistance of the nanowalls (relative to the nanocrystalline particle surface) might be attributed to the close-packed nature of its basal-plane face of the nanowalls. Such possibility is reminiscent of other well-known hcp (Hexagonal Close-Packed) crystal, i.e. graphite, where the similar electrochemical inactivity of the basal planes, relative to that of the prismatic planes, is well-documented [27,28].

For further quantitative estimation of the HER performance, the equilibrium reaction rate, i.e. the Tafel slope (b , Table 2) was calculated from the Tafel plot (Fig. 8a) [29,30], employing the Butler-Volmer equation and approximate Tafel equation. Remarkably, the Tafel slope of the nanowall sample was comparable to the best two data on the non-doped WC nanoparticles in the literatures [12,13]; the onset potential was one of the best in the list (Table 2). The overpotential change was also excellent; the acidic media employed in the present study was among the strongest (0.5 M H₂SO₄) listed in Table 2, and the employed cycles was the longest, while the employed potentials were similar. Remarkably,

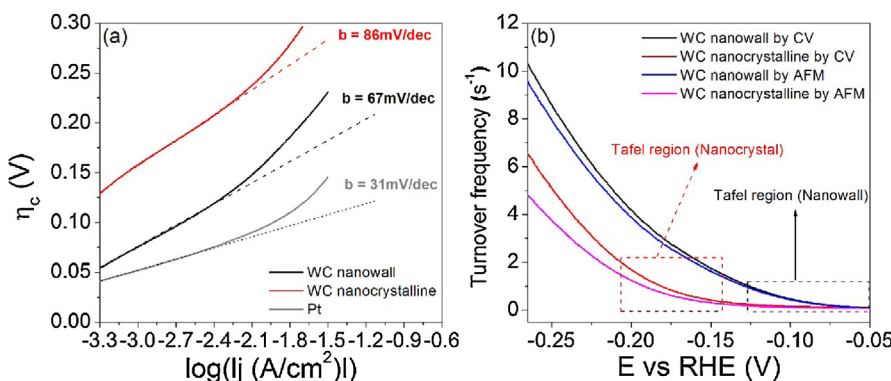


Fig. 8. (a) Tafel slope and (b) turnover frequency (TOF) of WC nanowall and nanocrystalline films within the Tafel region.

even under such harsh condition, the overpotential of the nanowall sample did not deteriorate at all. In addition, it was important that the small b value (67 mV/dec) of the nanowall sample indicated an intermediate reaction path between the Volmer-Heyrovsky (rds) and the Volmer (rds)-Heyrovsky mechanism (Statement S2) [10].

The exchange current density (j_0) is known to represent the HER activity, but it fails to reflect the effect of the porosity or surface roughness, which might induce the discrepancy of the active surface area from the geometrical surface area. A better choice for the figure of merit is the turnover frequency (TOF): the number of hydrogen molecules generated per active site and unit time. Assuming that cathodic current comes exclusively from HER, TOF is given as j/nFN (n : stoichiometric number of electron = 2, F : faraday constant = 96500, N : number of active sites) [31]. Assuming uniform isotropic distribution of the nanowalls in the film, N is given as follows: $N = \text{surface roughness factor } (R_f) \times (\text{Avogadro's number } (N_A) \times \text{film density } (\rho) / \text{formula weight of WC } (M_f))^{2/3}$. When the film surface is rough, its density (ρ) is difficult to analyze by x-ray reflectivity or ellipsometry, as for the present nanowall sample. Therefore we employed alternative technique: sample weight measurement by microbalance, followed by sample volume calculation from the film thickness (measured from SEM image) times sample area; it gave the density of 7.244 g/cm^3 for the nanowall sample, much lower relative to that of the solid tungsten carbide in the literature (15.6 g/cm^3) [32], obviously due to its porous structure (Fig. 4). For a flat surface ($R_f = 1$), the number of active site was estimated to be $7.91 \times 10^{14}/\text{cm}^2$. By contrast, for the nanowall sample (Fig. 4), the roughness factor was much larger, so that it dominated the N value. The R_f value was obtained by two different techniques: (1) surface roughness measurement by AFM; (2) the double layer capacitance (C_{dl}) measurement by CV (Statement S3). The measured surface roughness (rms value) was 19.8 nm for the nanowall sample, which gave N value of $1.57 \times 10^{16}/\text{cm}^2$ (Fig. S18: AFM image). Assuming that the C_{dl} was in proportion to the active surface area, C_{dl} ratio of the nanowall to the nanocrystalline sample also gave the roughness of the former. The measured C_{dl} for the nanowall sample was $367\text{ }\mu\text{F/cm}^2$ (Fig. S19), assuming that the double layer capacitance of the underlying nanodiamond film (substrate) was negligible. This value was 18.35 times larger than that of the solid bulk WC ($20\text{ }\mu\text{F/cm}^2$) [33], so that $R_f = 18.35$ for the nanowall sample, which eventually gave N value of $1.45 \times 10^{16}/\text{cm}^2$.

Fig. 8b shows the turnover frequency (TOF) calculated as in the preceding paragraph; the location (potential) of the Tafel region varied in proportion to the onset potential (Fig. 8a). While the TOF was an important figure of merit, there was no relevant data available for the WC material. Hence we took those of the Molybdenum sulfide, which was the best known non-precious metal catalyst for HER reaction, for comparison (calculation procedure: Statement

S3; Table S1: the TOF values as represented by the overpotential for $1\text{H}_2/\text{s}$ TOF) [4]. It was remarkable that the overpotential of the present tungsten carbide nanowall sample was the lowest among the data listed in Table S1, except the Jaramillo *et al.*'s report which was slightly lower than ours [34]. It was remarkable that such simple approach employing the CVD-grown nanowall sample, which was free from sintering, oxidation, or cost-issues, enabled the superior durability and HER activity even without doping, post-treatments or additional templates, and removed the inconveniences relevant to the conventional approaches adopting nanoparticles.

4. Conclusions

The pristine tungsten carbide nanowalls remained extremely resistant to further oxidation in the HER environment, throughout the prolonged exposure of 10,000 cycles, even without additional functionalization or modification. Their electrochemical activity, as presented by Tafel slope and TOF, was as excellent as those of the best data in the literature. Such superior performance was attributed to the crystalline perfection extending from the interior to the atomically flat/smooth surface of the nanowalls, as well as to the nanoporous structure.

Acknowledgements

This work was supported by the institutional program grant (2E26370) from Korea Institute of Science and Technology. The authors are grateful to M.K. Cho (in Advanced Analysis Center, KIST) for the comments for TEM characterization.

Appendix A. Supplementary data

Supplementary data associated with this article can be found, in the online version, at <http://dx.doi.org/10.1016/j.apcatb.2016.10.085>.

References

- [1] J.O.M. Bockris, Int. J. Hydrogen Energy 27 (2002) 731–740.
- [2] J.R. Rostrup-Nielsen, R. Nielsen, Catal. Rev. 46 (2004) 247–270.
- [3] R. de Levie, J. Electroanal. Chem. 476 (1999) 92–93.
- [4] C.G. Morales-Guio, L.A. Stern, X.L. Hu, Chem. Soc. Rev. 43 (2014) 6555–6569.
- [5] P. Xiao, X.M. Ge, H.B. Wang, Z.L. Liu, A. Fisher, X. Wang, Adv. Funct. Mater. 25 (2015) 1520–1526.
- [6] L. Han, M. Xu, Y. Han, Y. Yu, S. Dong, Chemsuschem 9 (2016) 2784–2787.
- [7] S.T. Hunt, T. Nimmanwudipong, Y. Roman-Leshkov, Angew. Chem. Int. Ed. 53 (2014) 5131–5136.
- [8] L.H. Bennett, J.R. Cuthill, A.J. McAliste, N.E. Erickson, R.E. Watson, Science 184 (1974) 563–565.
- [9] Y. Zhong, X.H. Xia, F. Shi, J.Y. Zhan, J.P. Tu, H.J. Fan, Adv. Sci. 3 (2016).
- [10] W.F. Chen, J.T. Muckerman, E. Fujita, Chem. Commun. 49 (2013) 8896–8909.

- [11] J. Guo, Z. Mao, X. Yan, R. Su, P. Guan, B. Xu, X. Zhang, G. Qin, S.J. Pennycook, *Nano Energy* 28 (2016) 261–268.
- [12] Y. Zhao, K. Kamiya, K. Hashimoto, S. Nakanishi, *Angew. Chem. Int. Ed.* 52 (2013) 13638–13641.
- [13] W.F. Chen, J.M. Schneider, K. Sasaki, C.H. Wang, J. Schneider, S. Iyer, S. Iyer, Y.M. Zhu, J.T. Muckerman, E. Fujita, *Chemuschem* 7 (2014) 2414–2418.
- [14] M.J. Bowick, L. Giomi, *Adv. Phys.* 58 (2009) 449–563.
- [15] D.R. Mohapatra, H.J. Lee, S. Sahoo, W.S. Lee, *CrystEngComm* 14 (2012) 2222–2228.
- [16] H.J. Lee, H. Li, H. Jeon, W.S. Lee, *Diam. Relat. Mater.* 19 (2010) 1393–1400.
- [17] B. Fultz, J.M. Howe, *Transmission Electron Microscopy and Diffractometry of Materials*, Springer, 2013.
- [18] J.B. Joo, J.S. Kim, P. Kim, J. Yi, *Mater. Lett.* 62 (2008) 3497–3499.
- [19] S.S. Perry, H.C. Galloway, P. Cao, E.J.R. Mitchell, D.C. Koeck, C.L. Smith, M.S. Lim, *Appl. Surf. Sci.* 180 (2001) 6–13.
- [20] X.F. Yang, Y.C. Kimmel, J. Fu, B.E. Koel, J.G.G. Chen, *ACS Catal.* 2 (2012) 765–769.
- [21] A.T. Garcia-Esparza, D. Cha, Y.W. Ou, J. Kubota, K. Domen, K. Takanabe, *Chemuschem* 6 (2013) 168–181.
- [22] L. Priester, *Grain Boundaries: From Theory to Engineering*, Springer, 2012.
- [23] B. Fultz, H.N. Frase, *Hyperfine Interact.* 130 (2000) 81–108.
- [24] E.J. Mittemeijer, *Fundamentals of Materials Science*, Springer, 2010.
- [25] J.-F. Ganghoffer, *Thermodynamics of Surface Growth with Application to Bone Remodeling*, InTech, 2011.
- [26] Y.K. Luo, R.S. Qin, *Surf. Sci.* 630 (2014) 195–201.
- [27] D.A.C. Brownson, D.K. Kampouris, C.E. Banks, *Chem. Soc. Rev.* 41 (2012) 6944–6976.
- [28] H.V. Patten, M. Velický, R.A.W. Dryfe, *Electrochemistry of Carbon Electrodes*, Wiley-VCH Verlag GmbH & Co KGaA, 2015, pp. 121–162.
- [29] C.H. Hamann, A. Hamnett, W. Vielstich, *Electrochemistry*, 2nd ed., Wiley, 2007.
- [30] A.J. Bard, L.R. Faulkner, *Electrochemical Methods: Fundamentals and Applications*, Wiley, 2001.
- [31] S. Shin, Z. Jin, D.H. Kwon, R. Bose, Y.S. Min, *Langmuir* 31 (2015) 1196–1202.
- [32] W.M. Haynes, *CRC Handbook of Chemistry and Physics: a Ready-Reference Book of Chemical and Physical Data*, CRC Press, 2011.
- [33] H.J. Zheng, C.N. Ma, J.G. Huang, G.H. Li, *J. Mater. Sci. Technol.* 21 (2005) 545–548.
- [34] T.F. Jaramillo, K.P. Jorgensen, J. Bonde, J.H. Nielsen, S. Horch, I. Chorkendorff, *Science* 317 (2007) 100–102.
- [35] J.F. Lin, O. Pitkanen, J. Maklin, R. Puskas, A. Kukovecz, A. Dombovari, G. Toth, K. Kordas, *J. Mater. Chem. A* 3 (2015) 14609–14616.
- [36] D.J. Ham, R. Ganeshan, J.S. Lee, *Int. J. Hydrogen Energy* 33 (2008) 6865–6872.